S1 Methods

S1.1 Experimental set-up

This section contains a detailed description of the experimental set-up show in Fig. 1. The engine exhaust was sampled at the engine exit plane using a single point sampling probe. The sample flow was then split into three sampling lines: the PM line (for measurements of particulate matter, PM), the GenTox line (for the sampling of genotoxic compounds) and the Annex 16 line (for measurements of the gaseous emissions and smoke certification, as specified in the ICAO Annex 16, Volume-II (ICAO, 2017)). The PM line was diluted with dry synthetic air (dilution factor $\sim$ 1:10) to prevent water condensation and coagulation of the particles in the sampling line that transfers the sample flow to the instrumentation room. The system deployed for the measurement of non-volatile PM (nvPM) was compliant with the new ICAO standard (ICAO, 2017) and included an AVL Particle Counter (APC, AVL, 489) for particle number measurements, a Micro Soot Sensor (MSS, AVL, Model 483) to determine BC mass concentrations, and a CO2 analyzer (Thermo Fisher Scientific, Model 410I) to calculate the dilution factor and the emission indices. The PM line additionally hosted the measurements of the optical properties (as described in the main text), size distributions (with a Scanning Mobility Particle Sizer, SMPS, TSI, Model 3938), particle density (coupling a Differential Mobility Analyzer (DMA, TSI, Model 3080), a Centrifugal Particle Mass Analyzer (CPMA, Cambustion) and a Condensation Particle Counter (CPC, TSI, Model 3776)), as well as the filter sampler for EC/OC analysis (URG, Series 2000-30FVT), a TEM grids sampler (homebuilt) for the study of particle composition and morphology, and a cell exposure chamber (NAVICIT) to study aircraft particulate related health effects (Jonsdottir et al., under review). The standard gas-phase measurements in the Annex 16 line included total hydrocarbons (THC) by Flame Ionization Detection (Horiba, Model MEXA-1170FID), NOx/SO2/CO/CO2/O2 by Chemiluminescence Detection (CLD) and Non-dispersive Infrared Absorption (Horiba, PG-250), and NO/NO2/NOx by Chemiluminescence (Eco Physics, Model CLD-844 S hr). In addition, a homebuilt sampling system for Volatile Organic Carbon (VOC) was accommodated in the Annex 16 line to collect samples for Gas Chromatography-Mass Spectrometry (GC-MS) analysis.

S1.2 Filter samples for EC/OC analysis

The method for measuring EC and OC in PM samples collected on filters is based on the volatilization and oxidation of carbon containing PM components with thermal-optical correction for pyrolytic carbon (PC). Thermal-optical OC/EC analysis as performed using a Sunset Laboratory Inc. OC/EC instrument is a NIOSH recognized method for the determination of organic and elemental carbon on particulates collected on quartz fibre filters. To quantify the content of EC and OC in the samples collected on the quartz fibre filter, thermal volatilization and oxidation at defined temperatures are used. A modified NIOSH 5040 thermal optical transmittance protocol, summarized in Table S1 was used. The optical transmittance through the sample was used for the correction of pyrolysis of OC occurring during the temperature steps in inert carrier gas (Helium mode). In the He mode, the oven's temperature is increased stepwise up to a first maximum of 870 °C. OC either volatilizes from the filter, or chars on the filter and forms pyrolytic carbon. In the He/O_2 mode the quartz oven is first cooled to 550°C and a second temperature ramp with a final temperature of 930°C is used. In the He/O_2 mode, EC and PC oxidize off the filter. All gases evolved from the filter during He and He/O_2 mode are carried into a manganese dioxide oven where organic vapors are quantitatively converted to CO_2 gas. In the methanator oven CO_2 is quantitatively converted to methane and finally measured with a flame ionization detector (FID). The laser transmittance signal was used to correct pyrolysis of OC to PC, which can take place when OC is heated in the He mode. Not correcting for pyrolysis leads to an underestimation of OC and corresponding overestimation of EC. As the temperature ramp proceeds, the laser transmittance is monitored continuously. Any charring of the organic carbon results in a decrease of the transmittance signal of the laser, whereas it increases when EC and/or PC oxidize. Hence, the

correction determines the amount of carbon oxidizes in the He/O_2 mode that is necessary to return the transmittance signal back to the initial value before pyrolysis started. The split point is defined as the split point when the transmittance returns to the initial value. The primary assumption for this correction is that the particulate elemental carbon and the pyrolytically formed elemental carbon have the same absorption coefficient.

An important component of the measurement system is the incorporation of a fixed volume loop which is used to inject an internal standard (5% Methane in Helium) at the end of every analysis. Having every sample correlated to an internal standard, small variations in instrument performance are normalized and a very stable, repeatable analytical method for EC and OC results. Because there are no traceable primary reference materials available for EC and OC, calibration is limited to TC. The principal calibration of the analytical system is conducted via TC values provided by blank filter samples spiked with calibration solutions of pure organic compounds such as sucrose. Additionally external calibration gas injections with methane (testing the FID) and CO_2 (testing the methanator and the FID) were also used.

The detection limit of the thermal-optical OC/EC analyzer is 0.2 µg C cm^{-2} of filter.

Carrier Gas	Duration (sec)	Temperature (°C)
He	80	310
He	80	475
He	80	615
He	110	870
He	45	550
He/O_2	45	550
He/O_2	45	625
He/O_2	45	700
He/O_2	45	775
He/O_2	45	850
He/O_2	60	870
He/O_2	120	930
CalGas + He/O_2	120	No heat

Table S1. Modified NIOSH 5040 thermal-optical protocol used in this work. Note: An internal calibration is carried out at the end of each run oxidizing a known volume of methane (CH_4).

The EC/OC concentrations were calculated using three different split points (Auto Split; Oxygen Pt; 540s). Figure S1 shows the correlations between the EC mass and the photoacoustic measurement of BC mass with the MSS for the three split points. In our case, the split point was selected manually at 540 s based on operator expertise.
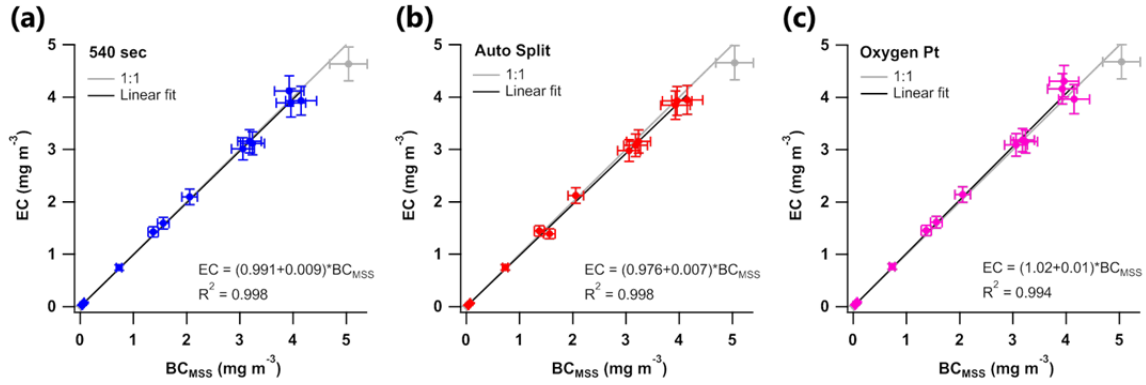
Figure S1. Correlation between EC mass concentrations measured with the Sunset OC/EC Aerosol Analyzer and the BC mass concentrations from the Micro Soot Sensor (MSS) when using (a) the manual split at 540 seconds, (b) the auto-split based on laser transmission, and (c) the Oxygen split point (which does not compensate for POC). Grey points indicate samples with a non-sharp limit of the sampling area that were therefore not used for the linear fit.

S1.3 Laboratory calibrations of the optical instruments

The optical instruments were calibrated in the laboratory prior to the measurements following standard operation procedures. The calibration particles (ammonium sulfate (AS) and nigrosin (Nig)) were generated with a TSI atomizer (model 306200) and diluted with HEPA filtered air to the desired mass concentrations (varied between 10 µg m^{-3} and up to 3 mg m^{-3}). After passing a silica-gel column for drying, the particle stream was divided into three different lines to a Scanning Mobility Particle Sizer (SMPS, TSI model 3080) to measure the size distributions of the particles, and the two optical instruments. The results of the calibrations are summarized in Fig. S2. As for high engine thrust levels the CAPS scattering signal in the diluted PM line is out of the instrument linear range (i.e. above 1000 Mm^{-1}), the scattering calibration was extended to the full measurement region (up to 6000 Mm^{-1}) and the calibration curve was used to correct the scattering measurements.
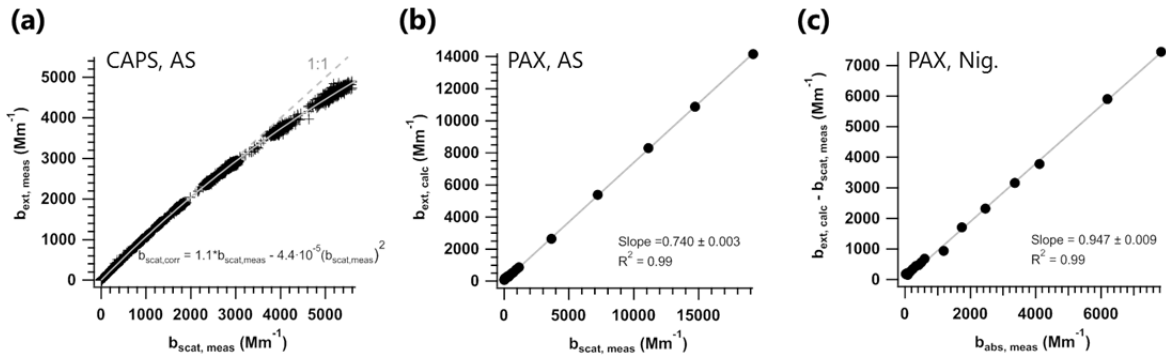

Figure S2. (a) CAPS scattering calibration using ammonium sulfate (AS). (b) PAX scattering calibration using ammonium sulfate (AS). (c) PAX absorption calibration using nigrosine ink (Nig).

In addition, a correction for the gas phase absorption is also required at the low measurement wavelength of the CAPS (532 nm). Under standard operation, the CAPS performs periodic baselines (i.e. measurements with a particle filter) to correct for the gas phase interference, which derives mainly from NO$_2$. This correction is critical in the study of aircraft emissions, as NO$_2$ levels vary between 0 and 30 ppm during typical jet engine operation and can fluctuate significantly in short timescales. Using the baseline function under such variable conditions can lead to inaccurate results. Therefore, we used the online NO$_2$ measurements in the Annex 16 line to correct for the gas phase interference. In order to calibrate the CAPS response to NO$_2$, laboratory measurements were performed using a NO$_2$ pressurized gas bottle (composition: NO$_2$ 20 ppm, O$_2$ 20 %, N$_2$ rest) diluted with HEPA filtered air. The results, presented in Fig. S3, reveal a very linear response (out to 6000 Mm^{-1}) for the CAPS extinction signal. The slope retrieved for the extinction measurement (3.2 ppb/Mm^{-1}) corresponds

to an absorption cross section for NO_2 at 532 nm of ~ $1.3 \cdot 10^{-19}$ cm^2, which agrees fairly well with previously reported values (Osthoff et al., 2006). Moreover, during the measurements of jet engine emissions, a bypass line with an HEPA filter was used to check the gaseous interferences in the CAPS at different thrust and NO_2 levels. In terms of light extinction, these results are in excellent agreement with the laboratory calibration curve. Regarding the scattering signal, this should in principle not be affected by the presence of NO_2. However, as shown in Fig. S3, the scattering signal increased with NO_2 following a third order polynomial. Besides, the curves obtained from the laboratory calibrations and jet engine measurements did not agree in this case. A light leak in the instrument was considered a possible source of these inconsistencies. However, very similar NO_2 interference curves were obtained after the light sealing of the instrument was exchanged. Despite all our efforts, we could not find the origin of the interference in the CAPS scattering signal. The online NO_2 measurements in the raw exhaust line and the laboratory calibration curve were used to correct the CAPS extinction measurements. Although we also tried to use the NO_2 calibration results to correct the CAPS scattering measurements, the results were inconsistent with other instruments.
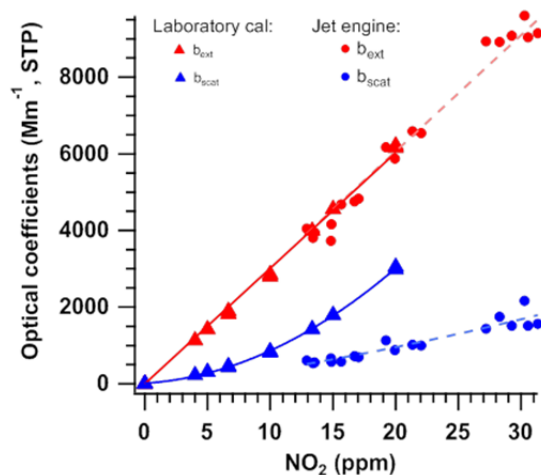

Figure S3. Calibration curves of the NO2 interference in the CAPS extinction and scattering channels from laboratory calibrations (with NO2 gas cylinder) and jet engine measurements (with HEPA filter in front of the instrument).

S1.4 Comparison with Mie Theory

To validate the results from the optical instruments, we compared the measurements of ammonium sulfate (AS) and nigrosin (Nig) at several concentrations with the optical coefficients modeled using Mie theory. For the modelling with Mie theory we used the log-normal fits of the SMPS size distributions and the ranges of literature refractive indexes (RI) reported in Table S2. The AS RI at 532 nm is in the range of 1.50-1.53 (see references in table), with imaginary part equal to zero (purely scattering). The RI of AS is known to be fairly constant over the range of measurement wavelengths deployed in this work, and therefore the same range of RIs was used to validate the measurements at 870 nm. Several works have measured the RI for Nig at 532 nm, which varies between $1.626+i0.243$ (Flores et al., 2012) and $1.728+i0.278$ (Bluvshtein et al., 2012), but none reported the RI at 870 nm. The spectroscopic ellipsometry measurements reported in Liu et al. (2013) and Bluvshtein et al. (2017) show a strong wavelength dependency of the Nig RI, with $1.6<n<1.8$ and $0.11<k<0.28$ for wavelengths between 200 and 800 nm.

Refractive index (RI=n+ik)	n	k	λ (nm)	Reference
Ammonium sulfate (AS)	1.53	1x10-7	532	Toon et al. (1976)
	1.53	0	532	Pettersson et al. (2004)
	1.52	0	532	Abo Riziq et al. (2007)
	1.521 ± 0.0026	0.002 ± 0.002	532	Dinnar et al. (2008)
	1.52 ± 0.01	0.00 ± 0.03	532	Lang-Yona et al. (2009)
	1.521 ± 0.004	0.000 ± 0.008	532	Bluvshtein et al. (2012)
	1.504 ± 0.015	0.000 ± 0.028	532	Flores et al. (2012)
Nigrosin ink (Nig)	1.67	0.26	532	Garvey and Pinnick (1983)
	1.70 ± 0.04	0.31 ± 0.05	532	Lack et al. (2006)
	1.649 ± 0.007	0.238 ± 0.008	532	Dinar et al. (2008)
	1.65 ± 0.01	0.24 ± 0.01	532	Lang-Yona et al. (2009)
	1.72 ± 0.01	0.28 ± 0.08	532	Lang-Yona et al. (2009)
	1.728 ± 0.009	0.278 ± 0.017	532	Bluvshtein et al. (2012)
	1.626 ± 0.021	0.243 ± 0.023	532	Flores et al. (2012)
	1.79*	0.22*	700	Liu et al. (2013)
	1.83*	0.14*	800	Bluvshtein et al. (2017)

Table S2. Literature refractive indexes (RI) of dry ammonium sulfate (AS) and nigrosin (Nig). *The reported RI for nigrosin at 700 and 800 nm were estimated from spectroscopic ellipsometry measurements.

Figure S4 shows the results of the comparison between modeled and measured scattering coefficient at several AS concentrations, using a range of RIs that slightly extends the lower limit of the RIs found in the literature. The color codes in panel (a) and (b) represent the slopes from the linear regression between the predictions from Mie theory varying RI ($1.46 \leq n \leq 1.53$ and k=0) and the measurements at (a) 532 nm and (b) 870 nm. At both wavelengths, the best results were found for RI=1.49+i0.00, for which both scattering measurements agree with Mie theory within 3 % (panels (c) and (d)). Our best estimate of the AS RI is slightly lower than the literature references in Table S2. This underestimation can be related to the use of the full size distributions instead of size- and mobility- selected particles, as recently shown in the work of Radney and Zangmeister (2018). However, the differences are very small, and good agreement (within 6 %) is still found using RI = 1.50 + i0.00. Therefore, we conclude that both instruments can accurately measure the optical coefficients of highly scattering particles.
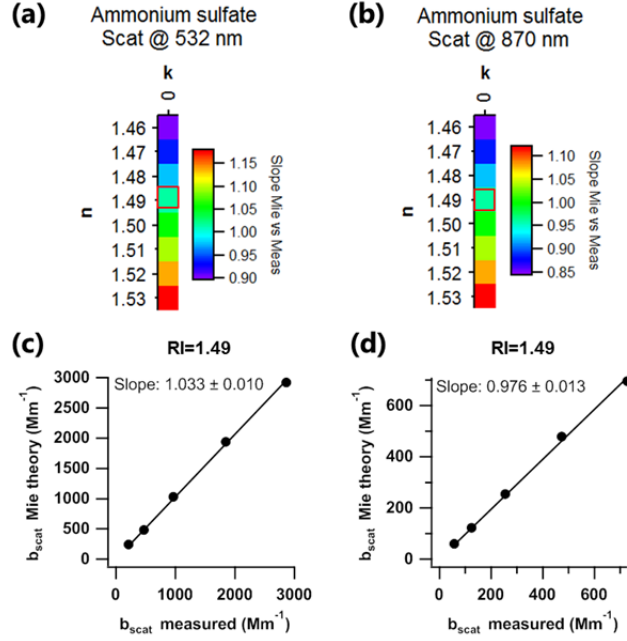
Figure S4. Comparison of the ammonium sulfate measurements with Mie theory; (a) Slope between modeled and measured b_{scat} at 532 nm varying the real part of the refractive index (RI=n+ik); (b) Slope between modeled and measured b_{scat} at 870 nm varying the real part of the RI; (c) Comparison of modeled and measured b_{scat} at 532 nm using our best estimate of the RI; (d) Comparison of modeled and measured b_{scat} at 870 nm using our best estimate of the RI.

The comparison with Mie theory for the measurements with nigrosin at 870 nm and 532 nm are shown in Figs. S5 and S6, respectively. In contrast to AS, in this case both the real and imaginary part of the RI had to be varied separately and the three optical coefficients (scattering, absorption and extinction) had to be considered for the comparison.

For the measurements at 870 nm, the best agreement with Mie theory predictions was obtained using RI=1.68 + $i0.10$ (Fig. S5 panels (a), (b), and (c)), for which the differences between the three modeled and measured optical coefficients was around 1 % (panels (d), (e), and (f)). Although we could not find literature values of the RI of nigrosin at this high wavelength, our best estimate for the Nig RI at 870 nm seems to be reasonable if compared to the trend at high wavelengths of the spectroscopic ellipsometry measurements reported in Table S2. Thus, our results seem to indicate that the PAX can accurately measure the optical coefficients of strongly absorbing particles.
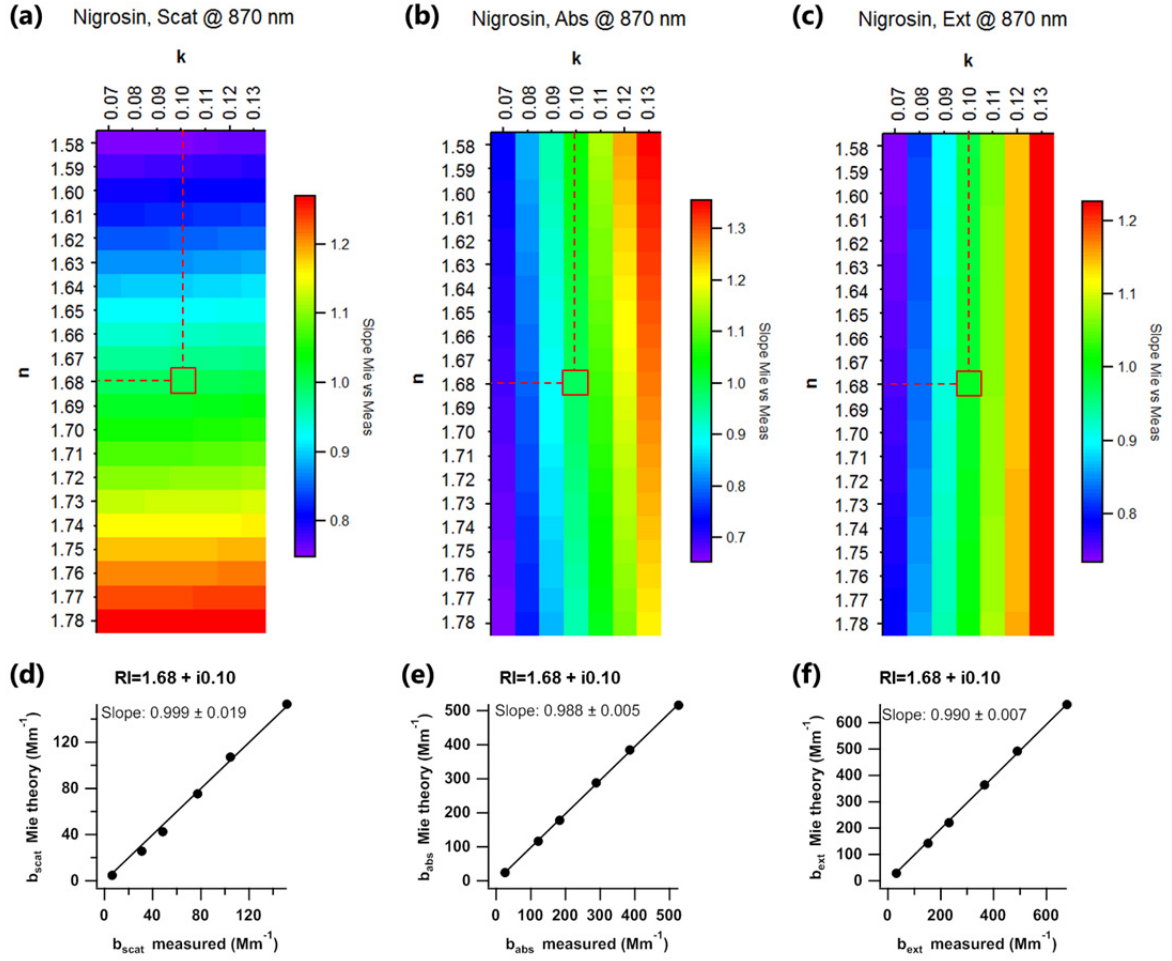
Figure S5. Comparison of the nigrosin measurements at 870 nm with Mie theory; (a) Slope between modeled and measured b_{scat} varying the refractive index (RI=n+ik); (b) Slope between modeled and measured b_{abs} varying the RI; (c) Slope between modeled and measured b_{ext} varying the RI; (d) Comparison of modeled and measured b_{scat} using our best estimate of the RI; (d) Comparison of modeled and measured b_{abs} using our best estimate of the RI; (e) Comparison of modeled and measured b_{ext} using our best estimate of the RI

At 532 nm, the comparison with Mie theory did not give such good results (Fig. S6). Although we extended the range of tested RIs to include all combinations of $1.60 \leq n \leq 1.75$ and *$0.20 \leq k \leq 0.35$*, Mie theory could not reconstruct the absolute values of measured scattering (underestimated by model) and absorption (overestimated by model). In contrast, the extinction measurement could be reproduced within 1 % using an RI = $1.60 + i0.22$. As for the AS experiments, this RI value is slightly below the literature range (both n and k), which can again be related to the use of the full size distributions in this work. To obtain a similar agreement for the scattering and absorption coefficients, a RI = $1.83 + i0.17$ has to be used, which largely differs from the literature values (unreasonably high n and low k). Thus, we conclude that for strongly absorbing particles the CAPS used in this work seems to properly measure the extinction, but overestimates the scattering (and consequently underestimates absorption).
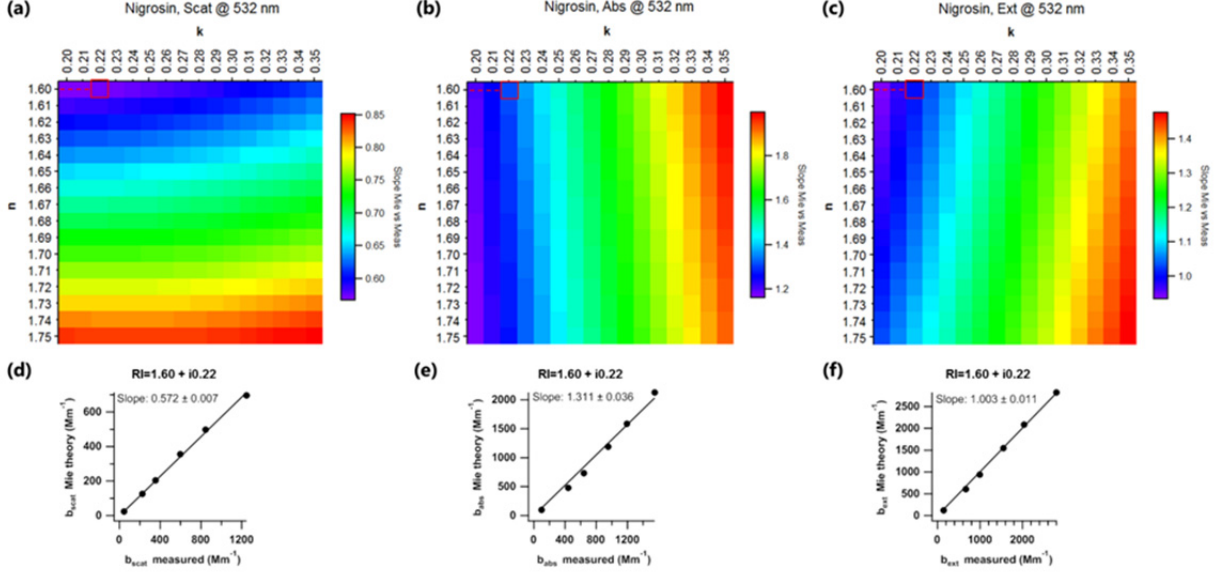
Figure S6. Comparison of the nigrosin measurements at 532 nm with Mie theory; (a) Slope between modeled and measured b_{scat} varying the refractive index (RI=n+*ik*); (b) Slope between modeled and measured b_{abs} varying the RI; (c) Slope between modeled and measured b_{ext} varying the RI; (d) Comparison of modeled and measured b_{scat} using our best estimate of the RI; (d) Comparison of modeled and measured b_{abs} using our best estimate of the RI; (e) Comparison of modeled and measured b_{ext} using our best estimate of the RI

As shown in the previous section, inconsistencies in the CAPS scattering signal were also observed in the NO_2 interference calibration. Despite all our efforts, we could not find the problem in the CAPS scattering measurement or a way to properly correct it. Therefore, we derived the CAPS scattering coefficient using the PAX absorption measurement and a thrust dependent absorption Angstrom exponent (AAE) obtained from aircraft engine measurements with a seven-wavelength aethalometer, as explained below.

S1.5 Calculation of scattering at 532 nm

The data from a 7-wavelength Aethalometer (model AE-33, Magee scientific) collected in a previous measurement campaign with the same type of engine (CFM56-7B/26) and Jet A-1 fuel, was used to estimate the absorption angstrom exponent (AAE) of the PM emissions at the engine exit plane. The AAE was calculated using the Aethalometer data at 520 nm and 880 nm, selected for being close to the CAPS and PAX operating wavelengths, as follows:

$$AAE = -\frac{\ln(\frac{b_{abs,520}}{b_{abs,880}})}{\ln(\frac{520}{880})} \tag{S1}$$

The power fit to the thrust dependent AAE reported in Fig. S7 was then used together with Eq. (S1) to derive the absorption coefficient at the CAPS measurement wavelength ($b_{abs,532}$) from the PAX absorption coefficient ($b_{abs,870}$). Lastly, the CAPS scattering was determined as the difference between the measured extinction and the calculated absorption at 532 nm.
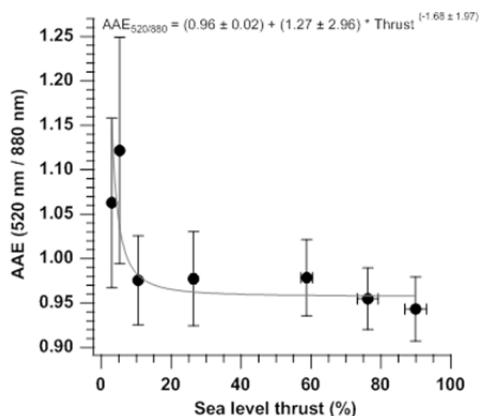
Figure S7. AAE thrust dependency determined from Aethalometer measurements at 520 and 880 nm.

S2 Results and discussion

S2.1 EC/OC analysis

Table S3 presents an overview of the results from the EC/OC analysis. While the concentration of EC in the back-up filters ($EC_{back-up}$) was negligible within the uncertainties, the positive artifact of gaseous OC adsorbing onto the filters surface ($OC_{back-up}$) represented around 43% of OC_{main} (see Fig. S8). The corrected OC concentrations (OC_{corr}) were calculated by subtracting $OC_{back-up}$ from OC_{main}, and OC_{corr} was then used to calculate the total carbon ($TC = EC_{main} + OC_{corr}$) and the OC fraction (OC/TC). Figure S9 shows the thermograms of the EC/OC analysis of the samples taken at low-, medium-, and high-thrust levels during measurements with Jet A-1 fuel.

	Thrust (%)	$OC_{back-up}$ ($\mu g\ m^{-3}$)	OC_{main} ($\mu g\ m^{-3}$)	OC_{corr} ($\mu g\ m^{-3}$)	$EC_{back-up}$ ($\mu g\ m^{-3}$)	EC_{main} ($\mu g\ m^{-3}$)	TC ($\mu g\ m^{-3}$)	OC/TC
Jet A-1	95.6	0.68 ± 0.13	1.64 ± 0.18	0.96 ± 0.22	-0.02 ± 0.10	4.63 ± 0.33	5.60 ± 0.39	0.17 ± 0.24
	77.4	0.49 ± 0.07	1.22 ± 0.11	0.72 ± 0.13	0.03 ± 0.05	3.01 ± 0.20	3.74 ± 0.24	0.19 ± 0.19
	64.0	0.24 ± 0.04	0.80 ± 0.07	0.56 ± 0.08	0.02 ± 0.03	2.10 ± 0.14	2.65 ± 0.16	0.21 ± 0.16
	52.7	0.11 ± 0.02	0.36 ± 0.03	0.24 ± 0.03	0.00 ± 0.01	0.74 ± 0.05	0.99 ± 0.06	0.25 ± 0.15
	28.8	0.08 ± 0.01	0.28 ± 0.02	0.20 ± 0.02	0.00 ± 0.01	0.06 ± 0.01	0.26 ± 0.03	0.78 ± 0.16
	5.2*	0.04 ± 0.01	0.14 ± 0.01	0.10 ± 0.01	0.00 ± 0.01	0.01 ± 0.01	0.11 ± 0.01	0.90 ± 0.16
	2.7	0.15 ± 0.02	0.39 ± 0.03	0.24 ± 0.03	0.00 ± 0.01	0.08 ± 0.01	0.32 ± 0.04	0.75 ± 0.17
HEFA 32%	96.2	0.57 ± 0.08	1.19 ± 0.12	0.61 ± 0.14	0.01 ± 0.06	3.93 ± 0.26	4.55 ± 0.29	0.14 ± 0.24
	96.0	0.44 ± 0.08	1.14 ± 0.11	0.70 ± 0.14	0.01 ± 0.06	3.89 ± 0.25	4.59 ± 0.29	0.15 ± 0.21
	94.2	0.78 ± 0.12	1.54 ± 0.16	0.76 ± 0.20	0.00 ± 0.09	4.12 ± 0.29	4.88 ± 0.36	0.16 ± 0.28
	85.1	0.35 ± 0.06	0.91 ± 0.09	0.57 ± 0.11	0.00 ± 0.05	3.12 ± 0.20	3.69 ± 0.23	0.15 ± 0.20
	83.2	0.44 ± 0.07	1.00 ± 0.09	0.55 ± 0.12	0.00 ± 0.05	3.16 ± 0.21	3.71 ± 0.24	0.15 ± 0.22
	63.3	0.20 ± 0.03	0.51 ± 0.05	0.32 ± 0.06	0.00 ± 0.02	1.59 ± 0.10	1.91 ± 0.12	0.17 ± 0.19
	62.5	0.36 ± 0.04	0.68 ± 0.05	0.31 ± 0.07	0.02 ± 0.02	1.43 ± 0.09	1.74 ± 0.11	0.18 ± 0.22
	29.3	0.08 ± 0.01	0.23 ± 0.02	0.15 ± 0.02	0.00 ± 0.01	0.03 ± 0.01	0.18 ± 0.02	0.84 ± 0.17
	2.8	0.23 ± 0.03	0.60 ± 0.04	0.36 ± 0.05	0.00 ± 0.01	0.04 ± 0.02	0.40 ± 0.05	0.90 ± 0.19

*Integrated sample that includes 65 min of Jet A-1, 70 min of HEFA 5% and 70 min of HEFA 10%

Table S3. Overview of EC/OC analysis results.
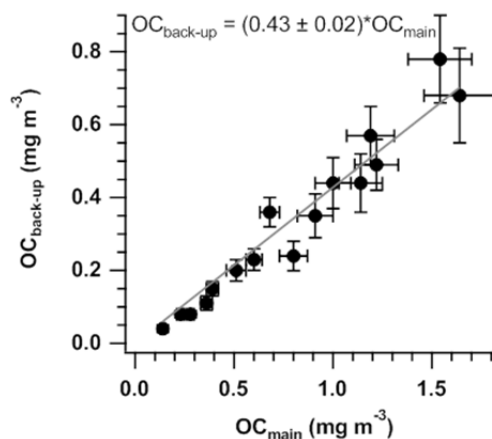

$OC_{back-up} = (0.43 \pm 0.02)*OC_{main}$

Figure S8. Correlation between OC measured in the back-up filter (positive artifact) and the main filter (positive artifact + real OC).
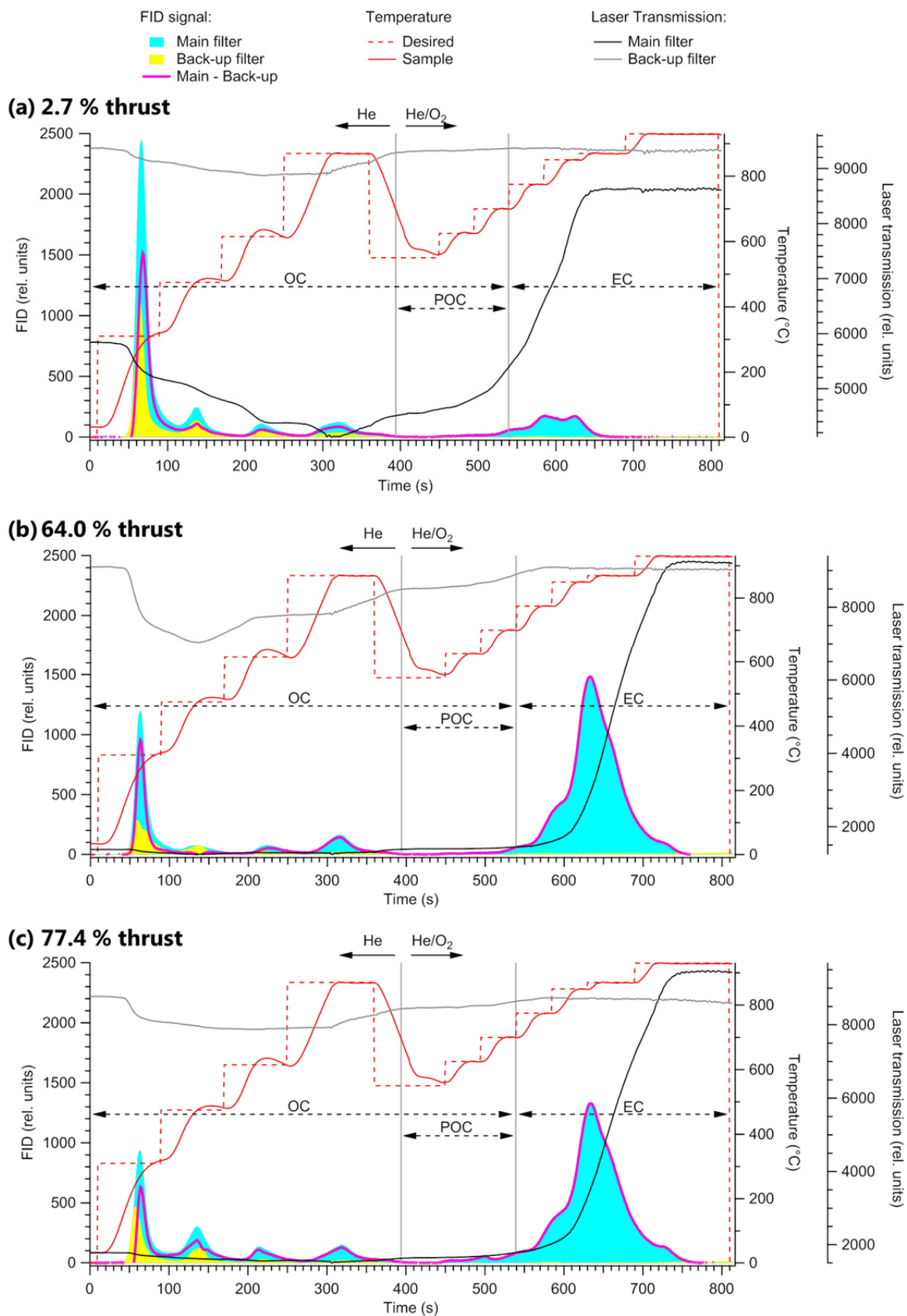
Figure S9. Thermograms of EC/OC analysis of aircraft PM samples for different thrust levels using Jet A-1 fuel; (a) 3 % thrust; (b) 64 % thrust; (c) 77 % thrust

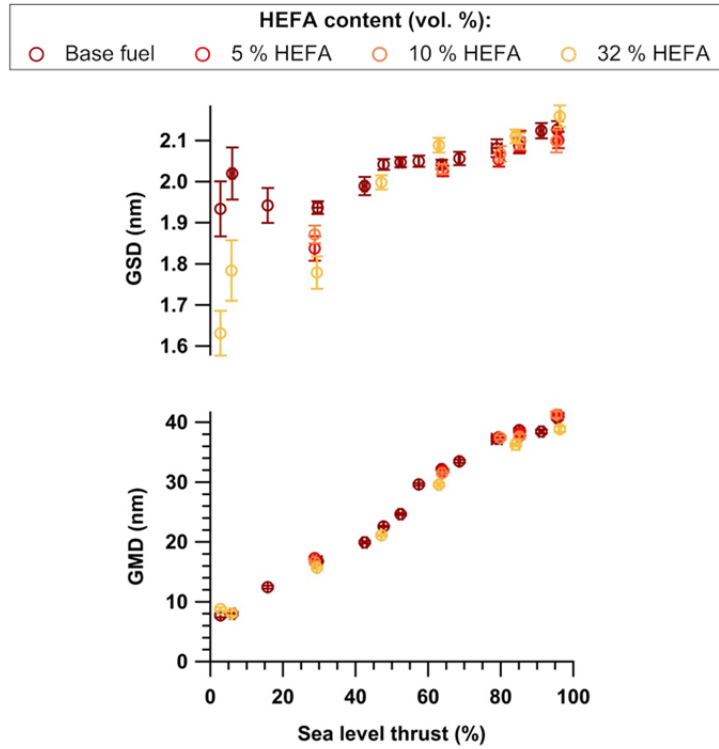## S2.2 Geometric mean particle diameter and geometric standard deviation

Figure S10. Geometric mean diameter (GMD, bottom) and geometric standard deviation (GSD, top) of the PM size distributions at the engine exit plane for different thrust levels and HEFA blends.
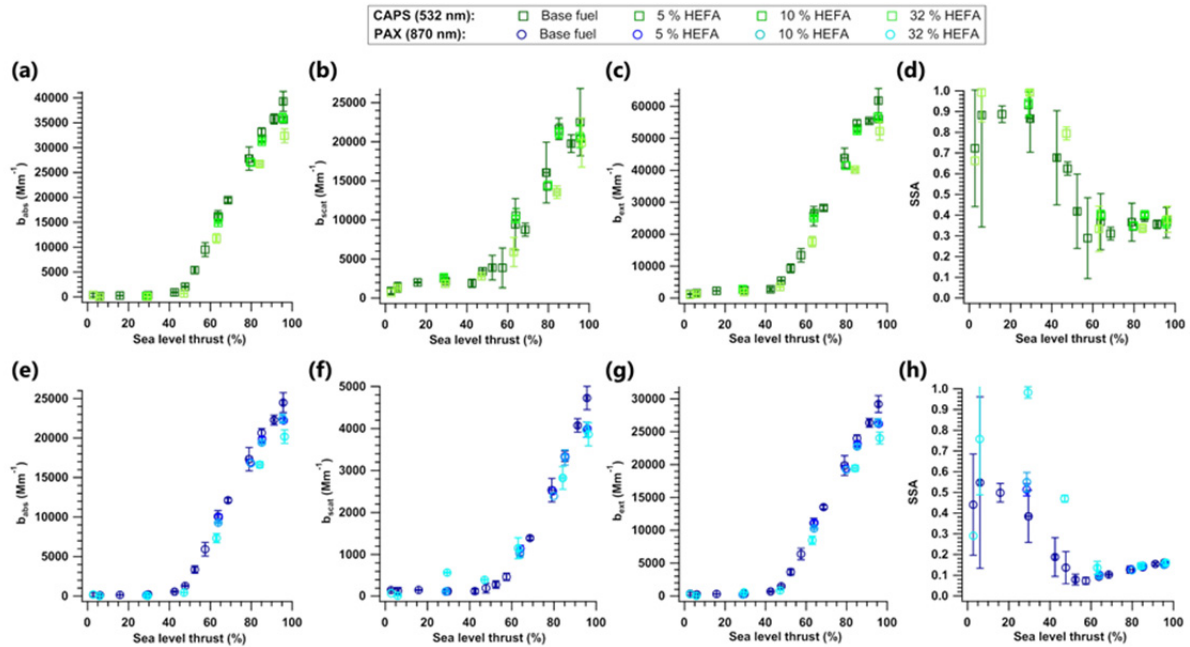
S2.3 Optical properties

Figure S11. Thrust dependency of the (a) absorption, (b) scattering, (c) extinction and (d) single scattering albedo (SSA) measured at 532 nm (CAPS) using Jet A-1 fuel and three HEFA blends. (e),(f),(g) and (h): same than above but for measurements at 870 nm (PAX).
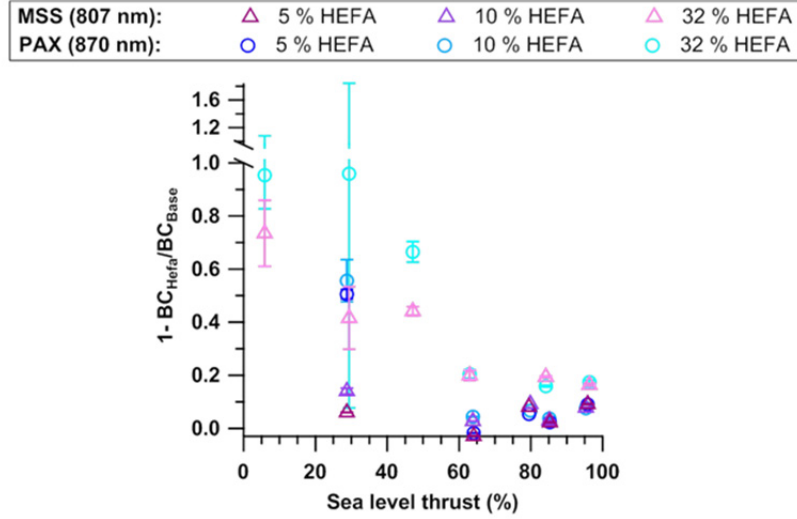
Figure S12. Thrust dependent decrease in BC$_{MSS}$ and BC$_{PAX}$ for the three HEFA blends in comparison to the base Jet A-1 fuel.
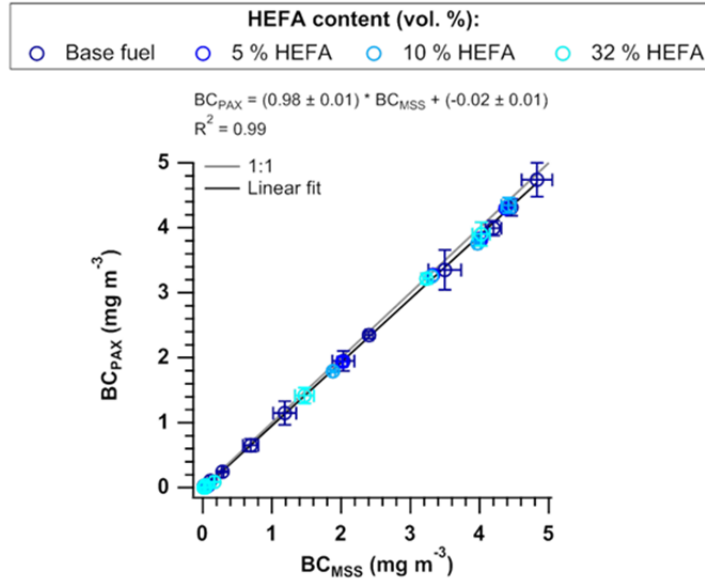

Figure S13. Correlation between BC$_{PAX}$ and BC$_{MSS}$ obtained with the different fuel blends.

S2.4 Radiative forcing

Figure S.13a reports the synthetic solar radiation spectrum at the top of the atmosphere from Gueymard et al. (2004), the direct normal radiation at cruise height (i.e. z=12 km) estimated with the SMARTS model (version 2.9.5, Gueymard, 2001), and the calculated atmospheric transmission (T_{atm}). The atmospheric conditions in the SMARTS model were defined using the 1976 U.S. Standard Atmosphere (United States Committee on Extension to the Standard Atmosphere, 1976); water vapor and ozone were calculated from the standard atmosphere at z=12 km; the reference gaseous absorption model was modified for the case of light pollution; the aerosol optical depth at 550 nm (τ_{550}) was calculated with the empirical relationship τ_{550}=exp(-3.2755-0.15078z) (valid for z > 6 km) following the recommendations in the SMARTS manual; and the absolute air mass was set to 1.5 (AIM1.5), corresponding to a solar zenith angle of 48.2° (temperate latitudes).
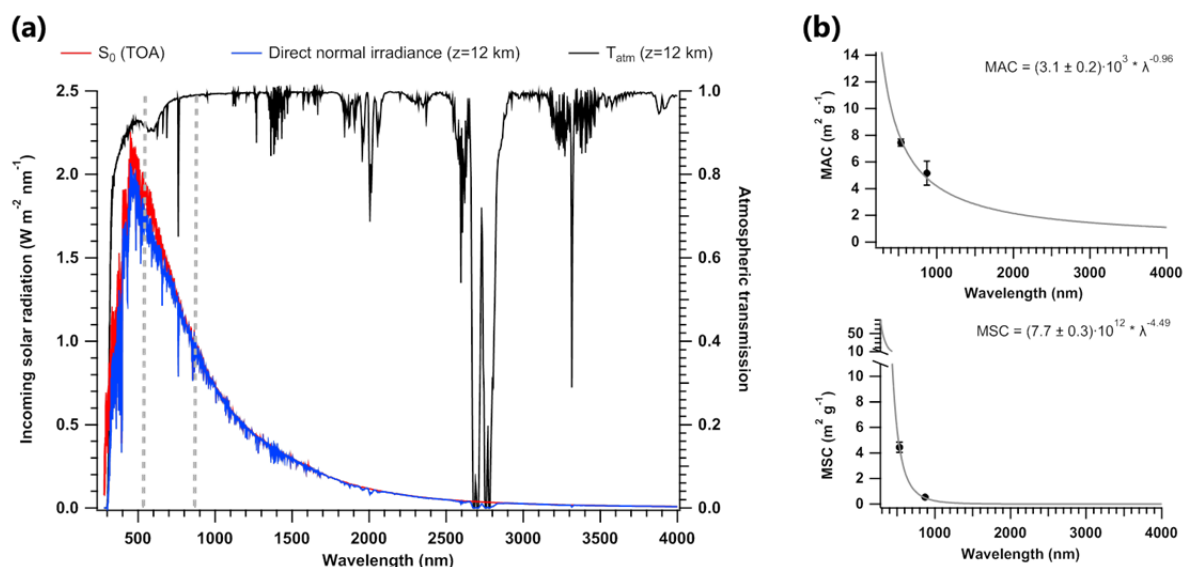
Figure S14. (a) Incoming solar radiation spectrum (S_0, Gueymard et al., 2004) and calculated direct normal radiation and atmospheric transmission (T_{atm}) at cruise height (b) Inverse wavelength fit to the mass absorption cross section (MAC, top) and mass scattering cross section (MSC, bottom) measured at 532 and 870 nm.

References

Abo Riziq, A., Erlick, C., Dinar, E., and Rudich, Y.: Optical properties of absorbing and non-absorbing aerosols retrieved by cavity ring down (CRD) spectroscopy, Atmos. Chem. Phys., 7, 1523-1536, doi:10.5194/acp-7-1523-2007, 2007.

Bluvshtein, N., Flores, J. M., He, Q., Segre, E., Segev, L., Hong, N., Donohue, A., Hilfiker, J. N., and Rudich, Y.: Calibration of a multi-pass photoacoustic spectrometer cell using light-absorbing aerosols, Atmos. Meas. Tech., 10, 1203–1213, doi:10.5194/amt-10-1203-2017, 2017.

Bluvshtein, N., Flores, J. M., Abo Riziq, A., and Rudich, Y.: An approach for faster retrieval of aerosols' complex refractive index using cavity ring-down spectroscopy, Aerosol Sci. Technol., 46, 1140-1150, doi:10.1080/02786826.2012.700141, 2012.

Dinar, E., Abo Riziq, A., Spindler, C., Erlick, C., Kiss, G., and Rudich, Y.: The complex refractive index of atmospheric and model humic-like substances (HULIS) Retrieved by a cavity ring down aerosol spectrometer (CRD-AS). Faraday Discuss., 137, 279–295, doi:10.1039/B703111D, 2008.

Flores, J. M., Bar-Or, R. Z., Bluvshtein, N., Abo Riziq, A., Kostinski, A., Borrmann, S., Koren, I., and Rudich, Y.: Absorbing aerosols at high relative humidity: linking hygroscopic growth to optical properties, Atmos. Chem. Phys., 12, 5511–5521, doi:10.5194/acp-12-5511-2012, 2012.

Garvey, D.M., and Pinnick, R.G.: Response characteristics of the particle measuring systems active scattering aerosol spectrometer probe (Asasp-X), Aerosol Sci. Technol., 2, 477-488, doi: 10.1080/02786828308958651, 1983.

Gueymard, C.: Parameterized transmittance model for direct beam and circumsolar spectral irradiance, Solar Energy, 71, 325-346, doi:10.1016/S0038-092X(01)00054-8, 2001.

Gueymard, C: The sun's total and spectral irradiance for solar energy applications and solar radiation models, Solar Energy, 76, 423-453, doi:10.1016/j.solener.2003.08.039, 2004.

ICAO: Annex 16 to the Convention on International Civil Aviation, Environmental Protection, Volume II Aircraft Engine Emissions, Fourth Edition, 2017.

Jonsdottir, H.R., Delaval, M., Leni, Z., Keller, A., Brem, B.T., Siegerist, F., Schönenberger, D., Durdina, L., Elser, M., Burtscher, H., Liati, A., and Geiser, M.: Non-volatile particle emissions from aircraft turbine engines at ground idle induce oxidative stress in bronchial cells, Under review.

Lack, D. A., Lovejoy, E. R., Baynard, T., Pettersson, A., and Ravishankara, A. R.: Aerosol absorption measurement using photoacoustic spectroscopy: sensitivity, calibration, and uncertainty developments, Aerosol Sci. Technol., 40, 697-708, doi:10.1080/02786820600803917, 2006.

Lang-Yona, N., Rudich, Y., Segre, E., Dinar, E., and Abo Riziq, A.:Complex refractive indices of aerosols retrieved by continuous wave-cavity ring down aerosol spectrometer, Anal. Chem., 81, 1762–1769, doi:10.1021/ac8017789, 2009.

Liu, P., Zhang, Y., and Martin, S. T.: Complex refractive indices of thin films of secondary organic materials by spectroscopic ellipsometry from 220 to 1200 nm, Environ. Sci. Technol., 47, 13594–13601, doi:10.1021/es403411e, 2013.

Osthoff, H. D., Brown, S. S., Ryerson, T. B., Fortin, T. J., Lerner, B. M., Williams, E. J., Pettersson, A., Baynard, T., Dube, W. P., Ciciora, S. J., and Ravishankara, A. R.: Measurement of atmospheric NO2 by pulsed cavity ring-down spectroscopy, J. Geophys. Res., 111, D12305, doi:10.1029/2005JD006942, 2006.

Pettersson, A., Lovejoy, E. R., Brock, C. A., Brown, S., and Ravishankara, A. R.: Measurement of aerosol optical extinction at 532 nm with pulsed cavity ring down spectroscopy, J. Aerosol Sci., 35, 995–1011, doi:10.1016/j.jaerosci.2004.02.008, 2004.

Radney, J. G., and Zangmeister, C. D.: Comparing aerosol refractive indices retrieved from full distribution and size- and mass-selected measurements, J. Quant. Spectrosc. Radiat. Transf., 220, 52-66, doi:10.1016/j.jqsrt.2018.08.021, 2018.

Toon, O. B., and Pollack, J. B.: The optical constants of several atmospheric aerosol species: ammonium sulfate, aluminum oxide, and sodium chloride, J. Geophys. Res. Atmos., 81, 5733-5748, doi: 10.1029/JC081i033p05733, 1976.

United States Committee on Extension to the Standard Atmosphere, "U.S. Standard Atmosphere, 1976", National Oceanic and Atmospheric Administration, National Aeronautics and Space Administration, United States Air Force, Washington D.C., 1976.